



Morphology, Intensity, and Rainfall Production of MJO Convection: Observations from DYNAMO Shipborne Radar and TRMM

WEIXIN XU AND STEVEN A. RUTLEDGE

Department of Atmospheric Science, Colorado State University, Fort Collins, Colorado

(Manuscript received 1 May 2014, in final form 16 September 2014)

ABSTRACT

This study uses Dynamics of the Madden–Julian Oscillation (DYNAMO) shipborne [Research Vessel (R/V) *Roger Revelle*] radar and Tropical Rainfall Measuring Mission (TRMM) Precipitation Radar (PR) datasets to investigate MJO-associated convective systems in specific organizational modes [mesoscale convective system (MCS) versus sub-MCS and linear versus nonlinear]. The *Revelle* radar sampled many “climatological” aspects of MJO convection as indicated by comparison with the long-term TRMM PR statistics, including areal-mean rainfall (6–7 mm day⁻¹), convective intensity, rainfall contributions from different morphologies, and their variations with MJO phase. Nonlinear sub-MCSs were present 70% of the time but contributed just around 20% of the total rainfall. In contrast, linear and nonlinear MCSs were present 10% of the time but contributed 20% and 50%, respectively. These distributions vary with MJO phase, with the largest sub-MCS rainfall fraction in suppressed phases (phases 5–7) and maximum MCS precipitation in active phases (phases 2 and 3). Similarly, convective–stratiform rainfall fractions also varied significantly with MJO phase, with the highest convective fractions (70%–80%) in suppressed phases and the largest stratiform fraction (40%–50%) in active phases. However, there are also discrepancies between the *Revelle* radar and TRMM PR. *Revelle* radar data indicated a mean convective rain fraction of 70% compared to 55% for TRMM PR. This difference is mainly due to the reduced resolution of the TRMM PR compared to the ship radar. There are also notable differences in the rainfall contributions as a function of convective intensity between the *Revelle* radar and TRMM PR. In addition, TRMM PR composites indicate linear MCS rainfall increases after MJO onset and produce similar rainfall contributions to nonlinear MCSs; however, the *Revelle* radar statistics show the clear dominance of nonlinear MCS rainfall.

1. Introduction

The Madden–Julian oscillation (MJO) (Madden and Julian 1971, 1972) is the most remarkable intraseasonal concept in the tropics. The MJO has broad impacts on the global weather and climate (Lau and Waliser 2005; Zhang 2005, 2013) such as monsoon onset and rainfall variability (Lau and Chan 1986; Hendon and Liebmann 1990; Lawrence and Webster 2002), tropical cyclone frequency (Liebmann et al. 1994; Maloney and Hartmann 2000), tornado outbreaks (Thompson and Roundy 2013), ENSO (Zhang 2005; Lau 2012), and extratropical climate modes (Lin et al. 2009; L’Heureux and Higgins 2008). Despite decades of study, the MJO is not well understood and

therefore MJO prediction skill is limited, especially concerning initiation over the Indian Ocean (Bechtold et al. 2008; Kim et al. 2009; Vitart and Molteni 2010). Meanwhile, the MJO has been poorly simulated by several generations of general circulation models (GCMs) (Lin et al. 2006; Hung et al. 2013). To advance understanding of the oceanic and atmospheric processes governing MJO initiation, the Dynamics of the Madden–Julian Oscillation (DYNAMO) field campaign was carried out in the central Indian Ocean (CIO) region during the boreal fall and winter of 2011/12 (Yoneyama et al. 2013). DYNAMO deployed sounding networks, radars across a spectrum of wavelengths, aircraft, oceanographic instrumentation, and enhanced moorings (Yoneyama et al. 2013). One of the key DYNAMO hypotheses is that specific convective populations are essential to MJO initiation. DYNAMO is well suited for testing this hypothesis through providing continuous three-dimensional measurements of convective clouds, both precipitating and nonprecipitating.

Corresponding author address: Weixin Xu, Department of Atmospheric Sciences, Colorado State University, 3915 West Laporte Avenue, Fort Collins, CO 80521.
E-mail: wxinxu@atmos.colostate.edu

The DYNAMO field campaign observed three MJO events during the October 2011–March 2012 time period (Yoneyama et al. 2013; Gottschalck et al. 2013). Observations from multiwavelength and multiplatform (ground based, shipborne, and airborne) radars have been used to investigate the full spectrum of convective clouds during these MJO events. Feng et al. (2014) constructed a merged cloud–precipitation radar dataset from three radars (Ka, C, and S band) deployed on Addu Atoll (Gan Island, Maldives) to document both precipitating (i.e., shallow, congestus, and deep convective clouds) and nonprecipitating clouds (i.e., mid-level, cirrus, and anvil clouds). This dataset, together with radiosonde data, can effectively serve to study the role of shallow and congestus clouds in the initiation of the MJO (Feng et al. 2014). Based on S-band (S pol) radar measurements collected during DYNAMO, Zuluaga and Houze (2013) found that rainfall in MJO active periods was intermittent and occurred in episodes lasting 2–4 days. They examined the convective population within these rainfall episodes and showed that shallow convective echoes (SCE) and narrow deep convective cores (DCC), wide convective cores (WCC), and broad stratiform (BSR) systems were the most frequent prior to, during, and after the maximum rainfall, respectively. It is interesting that this convective transition pattern on the scale of 2–4 days is actually similar to that on the MJO scale observed by satellite remote sensing (Morita et al. 2006; Tromeur and Rossow 2010; Riley et al. 2011) and shipborne radar in DYNAMO (Xu and Rutledge 2014, hereafter XR14). In addition, convective systems in various stages of the MJO also exhibit different microphysical properties (Rowe and Houze 2014). Using the S-pol radar data, Powell and Houze (2014) found that precipitation area, radar echo-top height, and tropospheric humidity rapidly increase over approximately 3–7 days prior to the MJO onset. Based on shipborne radar measurements in DYNAMO, XR14 documented a longer period of convective deepening prior to MJO onset: about 10–15 days. This longer convective deepening period is consistent with atmospheric moistening time scales inferred from the DYNAMO sounding network (Johnson and Ciesielski 2013). XR14 further composited the ship-based radar data as a function of MJO phase and identified strong correlations between convective populations and environmental conditions, both evolving along the “recharge–discharge” process (Bladé and Hartmann 1993; Hu and Randall 1994; Kemball-Cook and Weare 2001). The precipitating cloud population consists of shallow isolated convective cells in suppressed phases, isolated deep convective systems two phases prior to MJO onset, deep organized MCSs in active MJO phases, and stratiform-dominant systems in decaying

phases. Guy and Jorgensen (2014) also found similar shallow-to-deep-to-stratiform evolution of convective systems from analysis of airborne Doppler radar observations of the November MJO event during DYNAMO.

Although the above studies have extensively examined the convective and microphysical properties of convective clouds across the MJO life cycle, their convective organization and precipitation morphology (e.g., linear or nonlinear, MCS or sub-MCS) have not been quantified. Convective organization has important effects on heating distributions, momentum transport, and surface fluxes. For example, squall lines accompanied by extensive stratiform precipitation have very different heating profiles from convective-only systems, as the corresponding latent heating profiles for the convective and stratiform components are distinctly different (Johnson 1984; Houze 1989; Tao et al. 1993). Previous studies have shown that convective momentum transport is a function of system organization, with upgradient transport in the line-normal direction and downgradient transport in the line-parallel direction (LeMone 1983; LeMone et al. 1984; Wu and Yanai 1994; Tung and Yanai 2002). Convection without linear organization does not show consistent momentum transport properties (LeMone 1983; LeMone et al. 1984). Furthermore, surface flux enhancement was observed to be much stronger in highly organized convective systems when linear squall lines preceded a region of extensive stratiform precipitation (Saxen and Rutledge 1998).

Various organizational modes of tropical convection can occur under different environmental conditions, predominantly influenced by vertical shear and convective available potential energy (CAPE) (Moncrieff and Green 1972; Keenan and Carbone 1992; LeMone et al. 1998; Johnson et al. 2005). These studies found that vertical shear in the lower-to-middle troposphere is key to the orientation of convective lines while CAPE determines convective intensity and longevity. Convective systems can take on different morphologies, such as linear convection in the form of a leading convective line with trailing stratiform precipitation (e.g., Houze 1977; Zipser 1977) or randomly distributed convective cells. There are many studies on the convective organization and environmental characteristics in the literature, based on observations from the Global Atmospheric Research Program (GARP) Atlantic Tropical Experiment (GATE; Cheng and Houze 1979; Barnes and Seickman 1984; Szoke and Zipser 1986), the Tropical Ocean Global Atmosphere Coupled Ocean–Atmosphere Response Experiment (TOGA COARE; LeMone 1983; LeMone et al. 1998; Rickenbach and Rutledge 1998, hereafter RR98), the South China Sea Monsoon Experiment (Johnson et al. 2005), the Equatorial Mesoscale Experiment

(Alexander and Young 1992), and experiments in northern Australia (Keenan and Carbone 1992; Keenan and Rutledge 1993). Recently, Liu and Zipser (2013) constructed a climatology of MCS morphology in the tropics and subtropics using 14 years of Tropical Rainfall Measuring Mission (TRMM) measurements. However, there are very limited studies focusing on the morphology of the MJO convection over the CIO where most MJOs initiate.

Zuluaga and Houze (2013) have examined the frequency of convective systems during the MJO active periods during DYNAMO with the organization of SCE, DCC, WCC, and BSR. Guy and Jorgensen (2014) have investigated the convective organization and dynamics using airborne radar data collected from the National Oceanic and Atmospheric Administration (NOAA) P-3 aircraft deployed in DYNAMO. They found that DYNAMO MCSs were organized more parallel to the low-level shear and produced weaker cold pools due to weaker updrafts compared to MCSs observed in TOGA-COARE. However, the NOAA P-3 data were only available for a single MJO event (November) and nine separate flight episodes; therefore, samples of convection were relatively limited (Guy and Jorgensen 2014). Despite this research, outstanding questions remain regarding convective organization and precipitation morphology over the CIO. For example, the relative frequency of non-MCS- versus MCS-scale systems has not been quantified, nor has the degree of convective organization (linear versus nonlinear), nor has the rainfall production by various convective modes. Collectively, the variability of these characteristics with MJO phase has also not been quantified. This study seeks to contribute knowledge in these areas. In addition, the DYNAMO-based analyses are placed in the context of the long-term satellite (i.e., TRMM) climatology. This study first describes a time series of precipitation morphology based on analysis of DYNAMO shipborne C-band radar measurements collected from the Research Vessel (R/V) *Roger Revelle*. DYNAMO observations are composited as a function of MJO phase and compared in detail to the convective climatology based on TRMM PR data.

2. Data and methodology

This study employs 15 years (1998–2012) of TRMM precipitation feature (PF) data (Liu et al. 2008) and 3 months (October–December 2011) of radar observations collected from the R/V *Roger Revelle* deployed during DYNAMO (Moum et al. 2014). The long-term TRMM PR statistics cover the main MJO time period (October–April) over a $10^\circ \times 10^\circ$ box centered on the

DYNAMO array (5°S – 5°N , 75° – 85°E). DYNAMO radar measurements are compared to the TRMM PR climatology from various perspectives, including convective organization, intensity, and rainfall production as a function of MJO phase.

a. TRMM data

1) TRMM 3B42 RAINFALL PRODUCT

The version 7 TRMM Multisatellite Precipitation Analysis (TMPA) 3B42 rain product (Huffman et al. 2007) is used to provide continuous rainfall time series and large-scale rainfall maps, since the TRMM satellite data are only available twice a day. The TMPA 3B42 data are available from 1998 to the present, from 50°S to 50°N . This dataset has 3-h temporal resolution and 0.25° spatial resolution and uses TRMM PR observations, passive-microwave measurements from low-Earth-orbiting satellites, infrared radiance measurements from geostationary satellites, and rain gauge data when available.

2) TRMM PF DATASET

We use the version 7 TRMM database, mainly observations from the precipitation radar (PR) (Kummerow et al. 1998), to provide climatological context for the DYNAMO ship radar data. PR measurements have been grouped into PFs at the University of Utah (Liu et al. 2008). By definition, PFs are identified as PR-derived near-surface raining clusters (or continuous radar pixels). The minimum detectable reflectivity of the PR is 17 dBZ (Kummerow et al. 1998), which therefore defines the echo boundary of PFs (Fig. 1a). After a PF is identified, three-dimensional PR observations within the column are grouped into the PF, including such variables as maximum 20-, 30-, and 40-dBZ echo-top heights, rainfall volume (2A25, Iguchi et al. 2009), convective and stratiform precipitation fractions (2A23; Awaka et al. 2009), and the overall precipitation area of the PF. Since the horizontal resolution of the PR is 4 km prior to orbit boost (August 2001) and 4.5 km after boost, this study includes only PFs greater than 100 km^2 (4–5 TRMM PR pixels).

b. DYNAMO R/V Revelle dataset

The R/V *Roger Revelle* (Moum et al. 2014) was deployed at the east-central site (0° , 80.5°E) of the DYNAMO sounding array over the CIO (Yoneyama et al. 2013). During DYNAMO, R/V *Revelle* made four cruises to the campaign area (XR14) from September 2011 to January 2012. This study only analyzes measurements taken from cruises 2, 3, and 4 during which time the DYNAMO observations were extensive and MJO events were sampled (Yoneyama et al. 2013). Data are not included when the

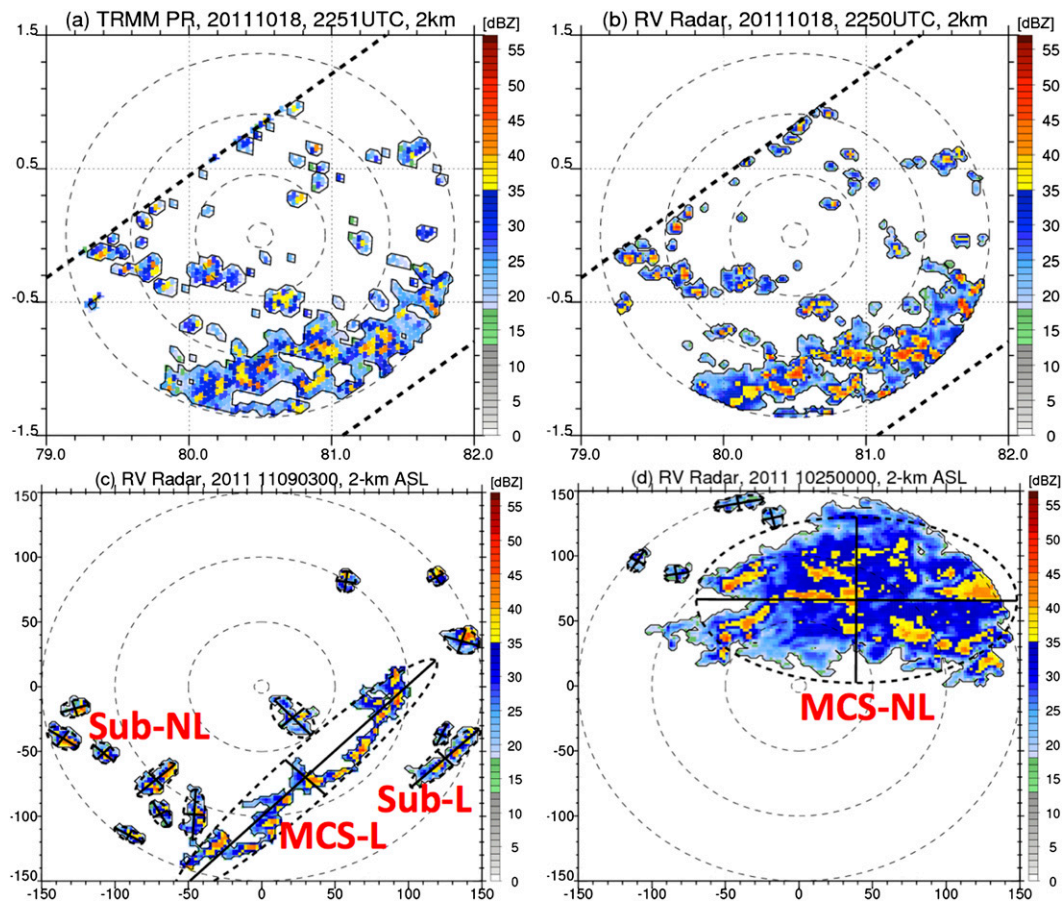


FIG. 1. (top) Examples of PFs (reflectivity > 17 dBZ at 2 km) observed by (a) TRMM PR at 2251 UTC 18 Oct 2011 and (b) *Revelle* radar at 2250 UTC 18 Oct 2011. (bottom) Examples of different morphologies of PFs measured by *Revelle* radar: (c) SubL (sub-MCS linear), SubNL (sub-MCS nonlinear), and MCS-L (MCS linear) at 0300 UTC 9 Nov 2011 and (d) MCS-NL (MCS Nonlinear) at 0000 UTC 25 Oct 2011. PFs in (c),(d) are fit into ellipses (dashed line) for major axis and minor axis (solid lines).

ship was transiting to/from port or otherwise off station. The vacancy of the *Revelle* had little influence on our results, since (fortunately) most of the missing data periods occurred during suppressed MJO phases with little if any rainfall. TRMM 3B42 rainfall time series over our analysis period are virtually identical when including and excluding data during the off-station periods (XR14).

1) RADAR DATA

The National Aeronautics and Space Administration (NASA) TOGA C-band radar on board the R/V *Revelle* (called the *Revelle* radar herein) operated round the clock when the ship was on station (XR14). The *Revelle* radar completed a full volume scan every 10 min including twenty-two 360° plan position indicator (PPI) sweeps and five vertical cross sections [range height indicator (RHI)]. This particular scanning strategy was set to provide continuous volume coverage and high-resolution 3D precipitating-cloud-structure information

(XR14). The *Revelle* radar data were calibrated and quality controlled by the Radar Meteorology Group at Colorado State University and NASA (details in XR14). After quality control, radar polar coordinate data were interpolated to Cartesian coordinates using the National Center for Atmospheric Research (NCAR) REORDER software package (Oye and Case 1995), with the resolution of 2 km in the horizontal and 0.5 km in the vertical (XR14). Radar reflectivity was then classified into convective and stratiform precipitation components based on Steiner et al. (1995). This algorithm only considers the horizontal texture of the radar reflectivity. Note that TRMM PR (2A23; Awaka et al. 2009) uses a somewhat more complicated technique that considers both horizontal and vertical gradients of reflectivity, as well as the existence of a reflectivity bright band. The rain rate–reflectivity (Z – R) relationship for convective rain is $Z = 134R^{1.44}$. For stratiform rain, $Z = 300R^{1.55}$ is used. These Z – R relationships (as well as the C-band attenuation

correction algorithm) were derived from drop size distribution measurement on Gan Island (DYNAMO) and Manus Island in the western Pacific (Thompson et al. 2014, manuscript submitted to *J. Atmos. Sci.*). Echo-top heights of specific echo intensities (e.g., 0 and 20 dBZ) are obtained by finding the maximum height of that value in the particular gridpoint column.

2) RADAR-BASED PFs

The echo object identification method used in the TRMM PF (Nesbitt et al. 2000; Liu et al. 2008) study was applied to the entire *Revelle* radar dataset. Specifically, radar PFs are defined as contiguous radar pixels exceeding the minimum TRMM PR detectable reflectivity (17 dBZ) at 2-km altitude (Fig. 1b). As a particular example, the *Revelle* radar observed nearly the same PF pattern as the TRMM PR (Figs. 1a,b). The three-dimensional radar measurements within the column are grouped into the PF. Therefore, radar PFs contain parameters such as maximum height of specific radar reflectivities (e.g., 20 or 30 dBZ), feature size (area of pixels greater than 20 dBZ), and the intensity, area, and volume of convective and stratiform precipitation. Again, radar PFs smaller than 100 km² (same rule applied to TRMM PFs) were not considered for analysis.

c. PF morphologies

The goal of this study is to quantify the frequency, intensity, and rainfall contributions of the MJO-associated convective systems as a function of convective organization (morphology). RR98 described the morphology of convection over the western Pacific warm pool using observations collected from the Massachusetts Institute of Technology (MIT) C-band radar on board the R/V *John V. Vickers* deployed during TOGA-COARE. RR98 divided echoes by sub-MCS versus MCS scales (less than or exceeding a length scale of 100 km) and whether the convective component was organized in a linear or nonlinear manner. We utilize a similar classification here. RR98 only assigned one organizational mode per radar volume, that being the mode with the largest size (MCS) and the highest degree of organization (linear). In contrast, this study utilizes an algorithm to automatically classify each PF, allowing multiple modes per radar volume. The algorithm applies elliptical fits to the area of PFs and calculates dimensions (e.g., major and minor axes) of the ellipses (Nesbitt et al. 2006; Liu and Zipser 2013). The major and minor axis lengths of the ellipse are derived from the mass distribution tensor eigenvalues of the raining points within each feature (Medioni et al. 2000; Nesbitt et al. 2006). First of all, PFs are separated into MCSs (area > 1000 km²) and sub-MCSs (area < 1000 km²) mainly

following the TRMM PR morphology studies (Nesbitt et al. 2000; Cifelli et al. 2007; Liu et al. 2008; Liu and Zipser 2013). This threshold of 1000 km² for the MCS category actually produces very similar MCS rainfall statistics (<10% difference) as the 100-km horizontal scale used by RR98 (not shown). MCSs and sub-MCSs are further defined as linear or nonlinear depending on the ratios of major to minor axes associated with each PF. RR98 defined the major-to-minor ratios of convective features (only considering convective components) greater than 5:1 as linear and ratios less than 5:1 as nonlinear. However, we define the major-to-minor ratios of PFs greater than 5:2 as linear and ratios less than 5:2 as nonlinear, considering that PFs (or precipitating area) are much broader than the embedded convective elements. Liu and Zipser (2013) also pointed out that the linear convection definition (ratios less than 5:1) is too restrictive for PFs. Sensitivity tests show that difference in rainfall statistics of linear or nonlinear MCSs is about 10% between the major-to-minor ratios of 5:1 and 5:2 definitions. Figures 1c,d provide examples of radar PFs in different morphology categories. Linear MCSs generally represent squall-line systems or convective cells arranged in a linear fashion (Fig. 1c), while nonlinear MCSs have randomly distributed cells embedded within stratiform precipitation (Fig. 1d).

d. MJO indices

This study employs the Wheeler–Hendon Real-Time Multivariate MJO (RMM) index (WH index; Wheeler and Hendon 2004) to define the MJO phase. The WH index is based on the combined empirical orthogonal functions (EOFs) of outgoing longwave radiation (OLR) and zonal wind fields at 850 and 200 hPa. The WH index has been widely used and is an effective filter for intraseasonal frequencies associated with the MJO (Lau and Wu 2010; Riley et al. 2011). Based on the WH index, each day in the tropics can be assigned to one of eight MJO phases. The active MJO phases over the CIO are assigned as phases 2 and 3. In other words, phases 1 and 4 respectively correspond to preonset and post-MJO periods in the CIO, while phases 5–8 are associated with suppressed MJO activity over this same domain. During the three MJO events in DYNAMO (October–December 2011), most of the days were of relatively strong MJO magnitude ($RMM1^2 + RMM2^2 > 1$), indicating significant MJO events (XR14). On the other hand, there were more than 50 MJO events observed by the TRMM satellite from October to April during 1998–2012. In compositing TRMM data as a function of MJO phase, we only include TRMM measurements taken during significant MJO periods (i.e., $RMM1^2 + RMM2^2 > 1.2$).

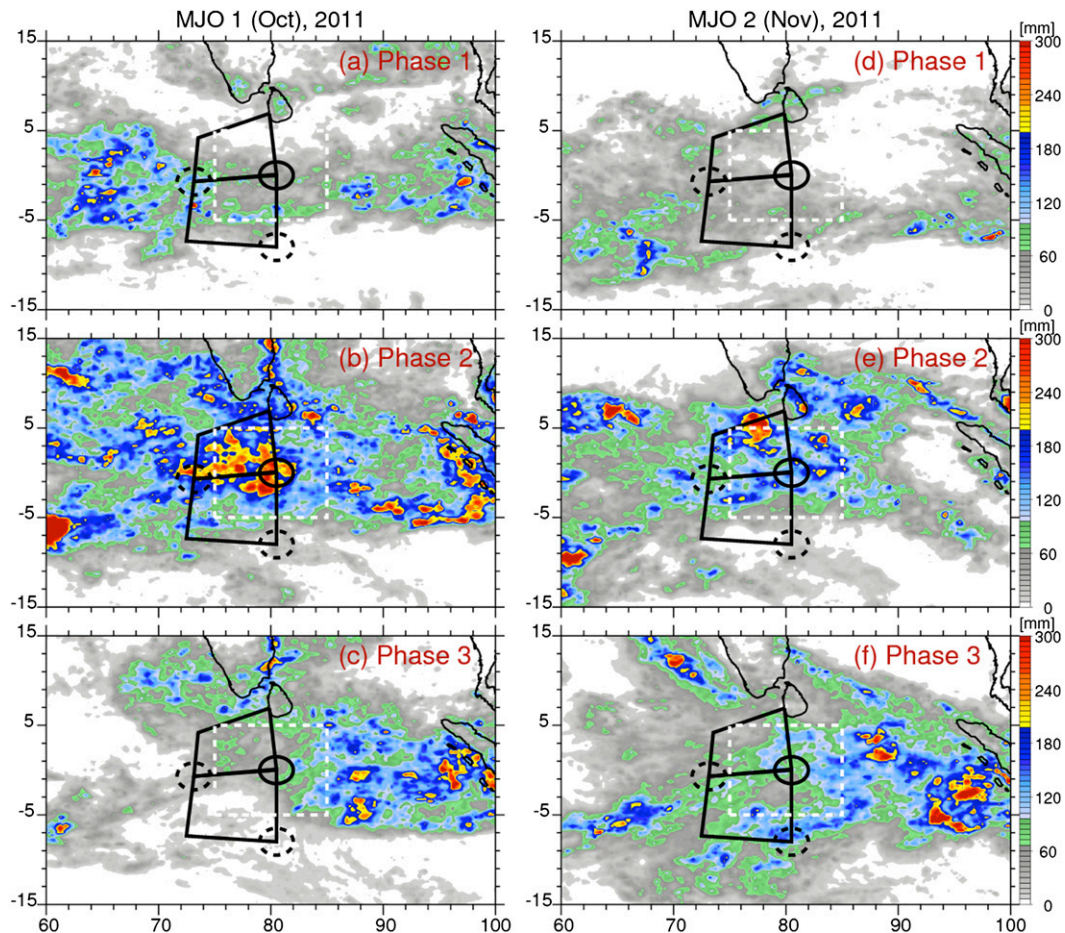


FIG. 2. Rainfall distribution (TRMM 3B42) over the Indian Ocean as a function of WH MJO phase. (a)–(c) During MJO 1 (phase 1: 15–19 Oct; phase 2: 20–29 Oct; phase 3: 30 Oct–3 Nov 2011) and (d)–(f) during MJO 2 (phase 1: 17–20 Nov; phase 2: 21–25 Nov; phase 3: 26–30 Nov 2011). The DYNAMO array is marked by the solid black line, while the white dashed box defines the climatology study region (5°S – 5°N , 75° – 85°E). DYNAMO radar ranges are marked by circles: *Revelle* radar (black solid), S pol on Gan Island (black dashed), and the C-band radar on R/V *Mirai* (black dashed).

3. Convective evolution of MJOs during DYNAMO

The DYNAMO field campaign observed two coherent MJO events and one incoherent (with incomplete cycle) MJO event (Yoneyama et al. 2013; Gottschalck et al. 2013; Johnson and Ciesielski 2013). The two coherent MJOs occurred in October (MJO 1) and November 2011 (MJO 2) with convection propagating from the CIO to the central Pacific and wind signals circumnavigating the globe (Gottschalck et al. 2013). Figure 2 clearly shows that the MJO heavy precipitation envelope initiated over the western Indian Ocean (Figs. 2a and 2d), passing through the DYNAMO array (Figs. 2b and 2e), and propagating eastward to the Maritime Continent (Figs. 2c and 2f). The prolonged rain event observed by the *Revelle* radar during MJO 1 (Figs. 2a–c) was associated with the

most intense portion of that particular MJO event. During MJO 2 (Figs. 2d–f), although intense precipitation was observed by the *Revelle* radar (Fig. 2e), the strongest convection and precipitation occurred over the northern portion of the large-scale DYNAMO array (Fig. 2e). The December MJO (MJO 3) was weaker in the OLR field accompanied by less coherent propagation in the wind component (Gottschalck et al. 2013). Only decaying phases (e.g., WH phases 4–5) were observed in MJO 3 as the more intense convection was located north of the *Revelle* radar coverage area (not shown).

Figure 3 shows time series of *Revelle* radar-estimated rainfall (3-hourly, areal mean) as a function of convective morphology during MJO 1 (Fig. 3a) and MJO 2 (Fig. 3b). (Because of the nature of the sampling for MJO 3, we do not consider MJO 3 for this time series analysis; however, we do include MJO 3 in the precipitation statistics

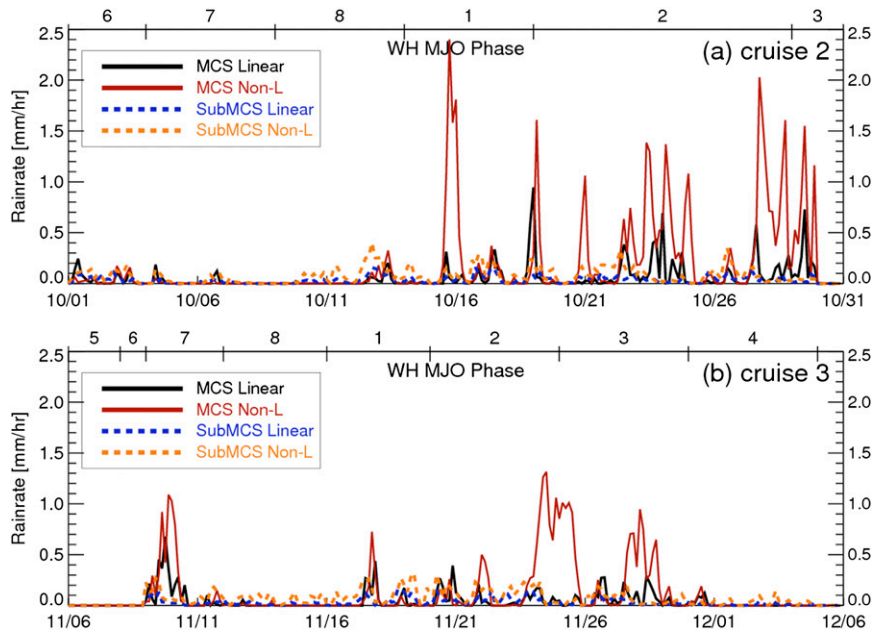


FIG. 3. Time series (3 hourly) of areal-mean rain rate (based on *Revelle* radar) as a function of different morphologies: (a) during R/V *Revelle* cruise 2 and (b) during R/V *Revelle* cruise 3. Corresponding WH MJO phase numbers are indicated on the top x axis.

described in more detail later.) The WH phase for each MJO is indicated at the top of each time-series panel. In general, suppressed periods (phases 5–7) in both MJO events were dominated by precipitation from sub-MCSs. During active periods (phases 2 and 3), frequent MCS (both linear and nonlinear) precipitation was present. These results are consistent with the evolution of precipitating cloud populations described by XR14. XR14 showed that deep convective cells frequently developed prior to MJO onset (i.e., during phase 1), but those cells rarely organized into mesoscale systems. Throughout the MJO cycle, sub-MCSs make minor contributions to precipitation (areal mean, 2–10 mm day⁻¹), roughly 5%–10% of that generated by MCSs (areal mean, 30–80 mm day⁻¹). However, sub-MCSs (or isolated convective cells) dominate the convective cloud population during DYNAMO and were suggested to play an important role in moistening the lower troposphere during MJO “recharging” periods (XR14). In terms of organizational mode, nonlinear MCSs contributed the most rainfall (20–60 mm day⁻¹), while linear MCSs produced only 20%–30% of that of the nonlinear MCSs (<25 mm day⁻¹).

During MJO active periods, MCS precipitation was more frequent and of higher intensity in MJO 1 than MJO 2 (Fig. 3, Table 1). As a result, the MJO envelope (active period) contained substantially more rainfall in MJO 1 (13.7 mm day⁻¹) compared to MJO 2 (9.3 mm day⁻¹; Table 1). This is also evident from the rainfall maps shown

in Figs. 2b and 2d. There were more than 10 major MCS precipitation events in MJO 1 (Fig. 3a). In MJO 2, there were only two major periods of MCS precipitation during active phases (Fig. 3b). These MCS precipitation events were associated with the passage of two Kelvin waves comprising MJO 2 (24 and 28 November; Gottschalk et al. 2013; Moum et al. 2014). Indeed, the precipitation morphology depicted here follows the evolution of echo-top height (0-dBZ radar echo top) as shown by XR14 (their Fig. 3b). For example, precipitating echo tops became substantially deeper around 16 October in MJO 1 and 21 November during MJO 2, when the dominant convective mode shifted to MCS precipitation (Fig. 3). This is reasonable since deep convective cells are necessary for MCS development. Prior to MJO onset, convective deepening (increase of the echo-top height) was more persistent and substantial in MJO 1 than in MJO 2 (XR14). After the MJO onsets, MCSs were more frequent and contributed more rainfall in MJO 1 than in MJO 2 (Fig. 3, Table 1).

4. Overall DYNAMO radar statistics and TRMM climatology

Based on echo object (or PFs) analysis, convective characteristics derived from 3 months of *Revelle* radar measurements are placed in the context of a 15-yr TRMM climatology (October–April) over the CIO (5°N–5°S, 75°–85°E; white box in Fig. 2). As detailed

TABLE 1. Rain depth (areal-mean rain rate) during MJO wet periods of MJO 1 (14–29 Oct) and MJO 2 (15–30 Nov). Fractions of rainfall contributed from systems of specific morphology category are also listed.

MJO envelope	Rain depth (mm day ⁻¹)	Linear MCS (%)	Nonlinear MCS (%)	Linear sub-MCS (%)	Nonlinear sub-MCS (%)
MJO 1	13.7	16	61	7	16
MJO 2	9.3	15	49	11	25

below, the 3-month-long *Revelle* radar-observed precipitation feature populations for the MJOs sampled during DYNAMO closely resemble the precipitation feature populations found in the TRMM PR 15-yr climatology (Table 2), comprising over 50 individual MJO events between 1998 and 2012. The 3-month, areal-mean rainfall rate recorded by the *Revelle* radar (7.0 mm day⁻¹) was also very close to that of the TRMM PR's 15-yr climatology (6.1 mm day⁻¹), which is also consistent with that derived from the multi-satellite rainfall product (3B42, 6.6 mm day⁻¹). It is interesting that DYNAMO recorded much higher daily rainfall compared to TOGA COARE (radar estimates of 4.5–4.8 mm day⁻¹; Short et al. 1997; RR98). This difference may owe to the fact that only one major MJO event occurred during TOGA COARE, while DYNAMO observed three MJO events during its (similar) duration. In fact, the 15-yr-averaged areal rainfall rate based on TRMM PR centered on the TOGA COARE large-scale domain (5°S–5°N, 140°–150°E) is 6.7 mm day⁻¹, which is very similar to that of DYNAMO. TRMM PR and the *Revelle* radar also observed very similar convective precipitation areas (25%–27%). However, there is a significant discrepancy concerning the convective rain volume fraction between TRMM PR (55%) and *Revelle* radar (73%). In fact, the convective rain fraction derived from *Revelle* radar (73%) is very close to that based on TOGA COARE shipborne radars (72%; Short et al. 1997; RR98). In contrast, Lin et al. (2004) reported a convective rain fraction of 40%–50% (or stratiform rain of 50%–60%) over the equatorial tropics based on a 5-yr TRMM PR climatology. The reason that the TRMM PR convective fraction is less than *Revelle* is due to the reduced resolution of the TRMM PR. For example, the convective (stratiform) fractions become 60% (40%)

when the *Revelle* radar data are reduced to a 4-km resolution. The coarser resolution of the TRMM PR relative to the *Revelle* radar does not allow it to resolve various reflectivity gradients that are characteristic of convection. We also need to emphasize that the convective–stratiform fractions derived from the *Revelle* data may not be generally representative of MJO precipitation since only MJO 1 made a “direct hit” on the *Revelle*'s location (Fig. 2), with the heaviest precipitation passing to the north of the *Revelle* during MJOs 2 and 3.

a. Morphology statistics

Even though the MJOs documented during DYNAMO passed through the *Revelle* radar area to various degrees, the cumulative function distribution (CDF) of *Revelle* radar PFs as a function of size is very close to that of the TRMM PR climatology (Fig. 4, red curves). This agreement suggests that during the 3-month observational period the *Revelle* radar did obtain a view of MJO convection that is representative of MJOs over this region of the CIO. Recall that the TRMM PR database contains over 50 MJO events. Although MCSs (PFs > 1000 km²) constitute only 10% of the total PF population, they contribute more than 70% of the total precipitation (Fig. 4, blue curves). This is quite common over the tropics (Nesbitt et al. 2000; Liu et al. 2008; Cifelli et al. 2007). Compared to the TRMM PR, the *Revelle* radar observed a smaller fraction of rainfall contributed by very large PFs (>50 000 km²). This may be due to the fact that the TRMM PR simply covers a larger swath area compared to the *Revelle* radar.

Figure 5 shows the PF frequency, contribution to total rainfall, and convective rain fraction in the four morphology categories. Error bars represent *t* test at the 95% significance level. Generally, the TRMM PR climatology

TABLE 2. Summary of total PF population, areal-mean rain rate, convective precipitation area percentage, and convective rainfall fraction observed by TRMM PR and the *Revelle* radar. Areal-mean rain rate derived from the TRMM 3B42 is listed in the parentheses. *Revelle* radar data are from October to December 2011, and TRMM PR data are during October–April from 1998 to 2012 over 5°S–5°N, 75°–85°E.

	Total PF samples	Areal-mean rain rate (mm day ⁻¹)	Convective area fraction (%)	Fraction of convective rain volume (%)
TRMM PR (3B42)	87 140	6.1 (6.6)	27	55
<i>Revelle</i> radar	77 408	7.0	25	73

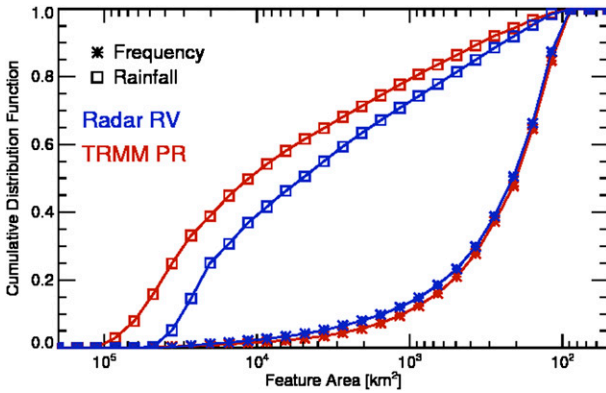


FIG. 4. CDF of PF population and rainfall fraction as a function of PF area. *Revelle* radar data (squares) are from October to December 2011, and TRMM PR data (stars) are selected over 5°S–5°N, 75°–85°E during October–April from 1998 to 2012.

and the *Revelle* radar statistics show similar distribution patterns as a function of PF morphology. They both indicate significant differences among different morphologies. The occurrence frequency (green bars in Fig. 5) is in the ascending order of linear MCSs (3%–5%), nonlinear MCSs (5%–7%), linear sub-MCSs (20%–25%), and nonlinear sub-MCSs (60%–65%). Obviously, the nonlinear sub-MCS mode dominated over the CIO in terms of frequency of occurrence. The linear MCS category was the least observed convective mode. In terms of rainfall contribution (blue bars in Fig. 5), nonlinear MCSs contributed about 50% of the total rainfall compared to linear MCSs which produced about 20% of the total rainfall. Similarly, sub-MCSs with linear organization contributed less rain (<10%) than nonlinear sub-MCSs (~20%). RR98, examining TOGA COARE shipborne radar data, reported that MCSs with linear organization dominated the total rainfall (80%), while nonlinear MCSs contributed less than 5% of the total rainfall. However, this study is PF based (multiple categories can appear in one radar image), while RR98 manually defined each radar image as having only one morphology mode defined as the convective feature with the highest degree of organization and size (i.e., the linear MCS is the largest and most organized mode). This study utilizes an objective algorithm (Nesbitt et al. 2006; Liu and Zipser 2013) to automatically identify each PF as one of the morphology categories, allowing systems of different morphologies (e.g., MCS and isolated convective cells) to be classified within the same radar image. In addition, RR98 classified on only convective components, while this study classifies on overall precipitation area of PFs. In fact, our analysis method yields very similar statistics when it is applied to the TOGA COARE MIT radar data (RR98) and TRMM PR measurements over a box of 1000 km × 1000 km over the TOGA COARE region

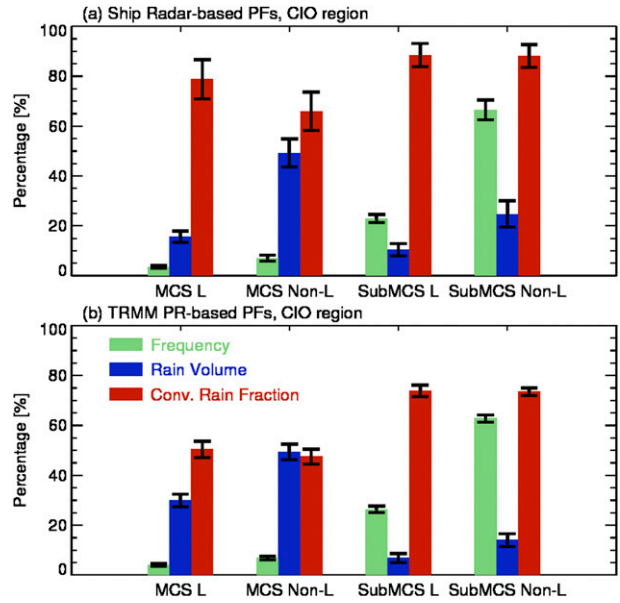


FIG. 5. Total PF frequency (green), fraction of total rain volume (blue), and convective rainfall fraction (red) of different morphology categories: (a) statistics from *Revelle* radar and (b) statistics based on TRMM PR. Error bars pass the *t* test at 95% confidence interval based on daily means.

(Fig. 6). Furthermore, our morphology statistics are consistent with the TRMM PR climatology across the broad tropical oceans—for example, there were 3 times more MCSs (PFs > 1000 km²) in the nonlinear mode compared to the linear mode (Liu and Zipser 2013). The assumptions made by RR98 (owing to the nonexistence of automated methods to objectively evaluate the large amount of radar data) led to a bias toward linear MCS systems.

The convective rainfall fraction was also calculated for each morphology category (red bars in Fig. 5). Concerning the statistics derived from the *Revelle* radar, sub-MCSs have larger fractions of convective precipitation (85%–95%) than MCS categories (60%–85%), indicating the more isolated and convective nature of the former category. The lower fraction of convective rain in MCSs is of course due to their substantial stratiform precipitation component. The convective rain fraction in DYNAMO MCS events ranges from 70%–85% for linear MCSs to 60%–75% for nonlinear MCSs. RR98 found an opposite trend for TOGA COARE event, with 66% for linear MCSs and 83% for nonlinear MCSs. Collectively, the convective fractions of DYNAMO events are also somewhat higher than several case studies of individual tropical squall lines from GATE [Houze (1977): 60%, Gamache and Houze (1983): 51%, and Houze and Rappaport (1984): 58%]. The comparison of these statistics needs to be done with caution since different

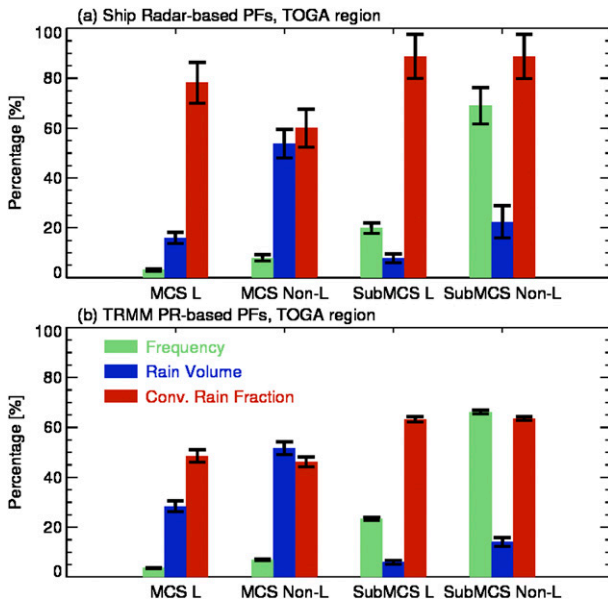


FIG. 6. As in Fig. 5, but for (a) MIT radar statistics during TOGA COARE and (b) TRMM PR statistics over the large TOGA COARE region (5°S – 5°N , 140° – 150°E) during October–April from 1998 to 2012.

analysis techniques were used (including different Z – R relationships for convective and stratiform rain; different convective–stratiform partitioning assumptions, etc.). Also, the present study represents a combination of many snapshot observations of MCS events while previous studies examined the entire life cycle of MCS events. Tropical squall lines over a portion of the system’s lifetime produced a broad range of convective rain fractions [Leary (1984): 70% and Zipser et al. (1981): 45%–50%].

It is important to point out that there are also differences in the morphology statistics between TRMM PR and the *Revelle* radar. For example, linear MCSs have higher rainfall contributions based on TRMM PR (28%) compared to the *Revelle* radar (15%). This may be partially due to the fact that the TRMM PR can detect longer line-shaped PFs (i.e., maximum of 1000 km along the PR swath in the study box) compared to the *Revelle* radar (i.e., maximum dimension of 300 km). As shown in Fig. 4, the TRMM PR observed a larger fraction of rainfall from extremely large PFs. On the other hand, the *Revelle* radar detected a larger rainfall fraction contributed from nonlinear sub-MCSs (23%) compared to that detected by the TRMM PR (12%). This may be due to the coarser native horizontal resolution of the TRMM PR data compared to the *Revelle* radar (4 km versus approximately 2 km). Furthermore, the convective rain fraction based on the *Revelle* radar is higher than that of the TRMM PR climatology regardless of morphology category. Again, differences in the native

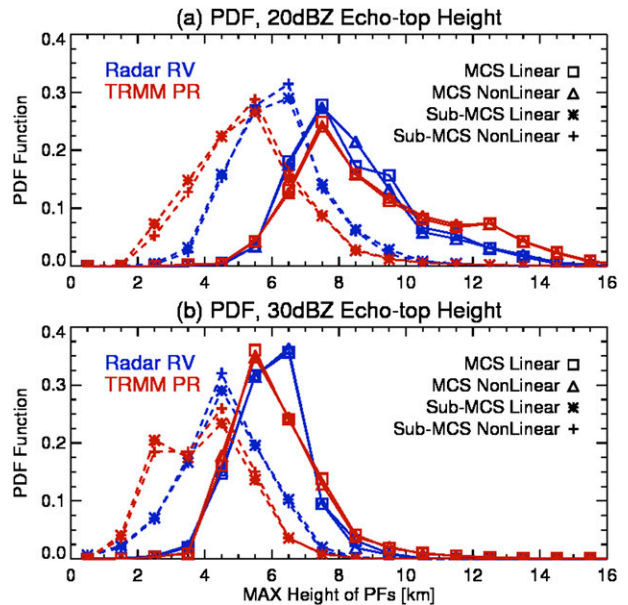


FIG. 7. PDFs of PFs categorized by (a) maximum 20-dBZ echo-top height and (b) maximum 30-dBZ echo-top height, based on *Revelle* radar (blue) and TRMM PR (red) measurements. Specific precipitation morphology of different categories is indicated by different markers.

data resolution are likely at play in explaining these differences.

b. Convective intensities

Figure 7 shows the probability distribution function (PDF) of 20- and 30-dBZ echo-top heights by convective mode—an indication of convective intensity. *Revelle* radar statistics are generally consistent with the TRMM PR climatology on echo-top heights of both 20 and 30 dBZ, with *Revelle*-observed PFs slightly taller (0.5 km) than those measured by TRMM PR. It is clear that MCSs persistently exhibited higher 20- or 30-dBZ echo tops than sub-MCSs, indicating that they contained stronger convective elements compared to convective elements in sub-MCSs. Rowe and Houze (2014) showed similar differences between MCSs and sub-MCSs over Gan Island during DYNAMO, in terms of 0-dBZ echo tops and frequency of large ice particles deduced from the NCAR S-pol radar polarimetric data. Liu and Zipser (2013) reported that organized convective lines across the broad tropics are slightly weaker than those with near-circular shapes, indicated by lower 30-dBZ echo-top heights and warmer 37-GHz brightness temperatures. However, this study indicated that convective systems over the CIO with linear and nonlinear organization have nearly the same convective intensities (e.g., 30-dBZ echo-top heights). In this study, the 20-dBZ echo-top heights of MCSs peaked at 7.5 km,

with approximately 10% of those systems achieving heights above 10 km (Fig. 7a). For MCS convective cores, the 30-dBZ echo-top-height mode was near 6 km, with a very sharp drop off above this altitude (Fig. 7b). Only 5% of the 30-dBZ echo tops exceeded 8 km, which is an effective threshold for lightning occurrence (Zipser 1994; Petersen et al. 1996).

Figure 8 depicts rainfall fractions contributed by each morphology type as a function of 20- and 30-dBZ echo-top height. Most of the MCS rainfall (70%–80%) was contributed from deep systems (e.g., 20-dBZ echo-top height greater than 10 km; Fig. 8a). Note that only 10% of the observed MCSs had 20-dBZ echo tops exceeding 10 km (Fig. 7a). Only 5% of the sub-MCS precipitation came from systems with 20-dBZ echo tops higher than 10 km. Approximately 10%–20% (2%) of MCS (sub-MCS) rainfall over the CIO was associated with intense convection—for example, 30-dBZ echo tops greater than 8 km (Fig. 8b). Xu and Zipser (2012) reported that over oceans less than 10% of rainfall was contributed by intense convection (e.g., 30-dBZ echo tops greater than 8 km or presence of lightning) compared to 70% over tropical continents. These findings are consistent with observed lightning frequencies presented by XR14.

There are notable differences in the rainfall contributions (as a function of convective intensity) between the *Revelle* radar and the TRMM PR climatology. The TRMM PR climatology suggests that more than 40% of the MCS rainfall was contributed by systems with extremely deep convective cores (e.g., 20-dBZ echo tops greater than 12 km), but the *Revelle* radar indicates only about 15% of MCS rainfall was due to MCSs with deep convective cores (Fig. 8a). In addition, TRMM PR climatology shows 20% of the MCS rainfall was associated with intense convection (30-dBZ echo tops greater than 8 km), while the *Revelle* radar shows only 10%. However, there was a larger fraction of sub-MCS rainfall contributed by PFs with relatively high echo tops (e.g., 20-dBZ echo tops greater than 8 km, or 30-dBZ echo tops greater than 6 km) as indicated by the *Revelle* radar compared to the TRMM PR climatology. Again, these discrepancies might originate from differences in rainfall estimation algorithms between TRMM PR and the *Revelle* radar, as the convective intensities are similar between *Revelle* statistics and TRMM PR climatology. It is possible that the TRMM PR underestimated rainfall for relative weak radar echoes but overestimated for strong radar echoes compared to the *Revelle* radar, since sub-MCSs should contain weaker radar echoes near the surface, owing to their substantially weaker convective intensities compared to MCSs (Fig. 7).

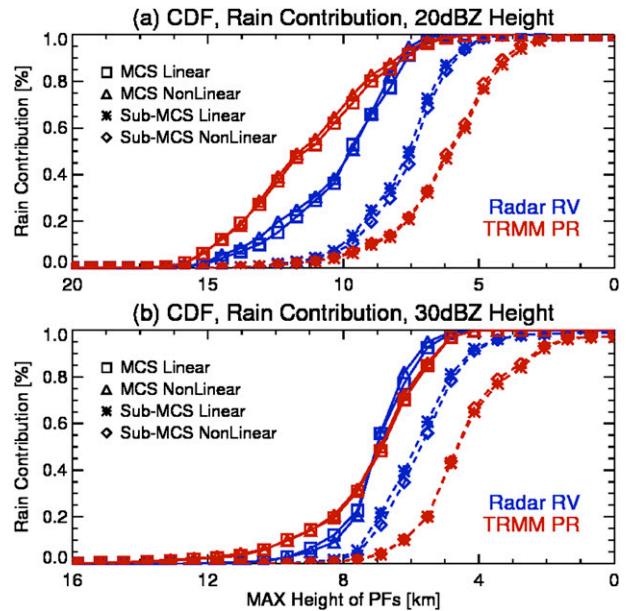


FIG. 8. CDFs of rain volumes contributed from different PFs categorized by (a) maximum 20-dBZ echo-top height and (b) maximum 30-dBZ echo-top height, based on *Revelle* radar (blue) and TRMM PR (red) measurements. PFs of specific precipitation morphology are indicated by different markers.

5. Composites as a function of MJO phase

XR14 showed that convective characteristics (i.e., precipitation amount, convective intensity, and lightning frequency) and environmental variables (SST, tropospheric humidity) evolved along the “recharge–discharge” processes (Bladé and Hartmann 1993; Kemball-Cook and Weare 2001). One of the major goals of this study is to examine how the precipitation morphologies vary with MJO evolution or MJO phase defined by the WH index. It is also important to know whether these MJO phase-based composites observed during DYNAMO are comparable to the TRMM PR climatological patterns. This section compares the three MJO events in DYNAMO against more than 50 MJO events observed by TRMM, from the perspectives of total rainfall, convective/stratiform rain fraction, precipitation morphology, and rainfall contribution as a function convective depth. There were more than 300 MJO event days in each MJO phase during October–April in 1998–2012. However, we only include major MJO event days (i.e., $RMM1^2 + RMM2^2 > 1.2$). Samples of selected MJO event days in each MJO phase and corresponding PF populations are listed in Table 3.

a. Total rainfall and precipitation types

Figure 9 shows the areal-mean rainfall derived from the *Revelle* radar, TRMM PR, and 3B42 estimates as

TABLE 3. Samples of MJO event days and PFs as a function of WH MJO phase in the TRMM PR and *Revelle* radar dataset. TRMM PR dataset includes measurements observed during October–April from 1998 to 2012 over the CIO (5°S–5°N, 75°–85°E). TRMM sampling for WH MJO composites only include significant MJO days (i.e., $RMM1^2 + RMM2^2 > 1.2$).

Phase	1	2	3	4	5	6	7	8
TRMM sampling days	138	189	227	187	234	231	194	180
TRMM PFs	4749	6177	6006	3586	5173	5276	4996	5757
<i>Revelle</i> sampling days	9	14	5	10	6	6	8	9
<i>Revelle</i> PFs	12 708	22 043	6645	9453	1406	1371	3699	10 538

a function of MJO phase. XR14 previously showed that *Revelle* radar-based rainfall time series agreed well with that from TRMM 3B42. Figure 9 indicates that the large-scale MJO phase-to-phase rainfall evolution pattern was also captured by the *Revelle* radar observations. For example, each rainfall plot shows a similar increasing trend from phase 7 to phase 2, maximum at phase 2, and a decreasing trend from phases 2 to 5. The MJO phase-composited rainfall evolution during DYNAMO (black, orange, and blue curves; Fig. 9) was higher than that of the TRMM PR climatology (red curve), especially during active phases of the MJO (e.g., phases 1–3). Note that because the TRMM PR provides very small data samples during the 3 months of DYNAMO (only two overpasses per day), 3B42 data are used to represent the satellite rainfall estimates during DYNAMO. Compared to the 3B42 product over the *Revelle* radar coverage area (orange curve), the *Revelle* radar (black curve) measured more rainfall during MJO building phases (e.g., phases 8 and 1) but less rainfall during MJO active and decaying phases (phases 2–4). This may result from the fact that TRMM 3B42 mainly relies on microwave and infrared measurements. Both microwave and infrared rainfall estimation techniques are based on indirect relationships between ice particles/cloud tops and the surface precipitation that vary greatly among different weather regimes. During the active and decaying phases, precipitation systems could still have abundant ice particles and extensive cold cloud tops, but precipitation intensity is substantially reduced owing to the weakening of convective intensity (XR14). In this case, microwave and IR techniques likely overestimate precipitation. These trends suggest that 3B42 may underestimate rainfall produced by deep isolated convective cells during MJO building phases and overestimate precipitation produced by large MCSs during active phases. Compared to 3B42 over the large-scale area (blue curve), the *Revelle* radar (black curve) diagnosed less rainfall during MJO active and decaying phases. This difference is likely caused by the heaviest precipitation passing to the north of the *Revelle* during MJOs 2 and 3. However, the main take-away message from the above is that the *Revelle* radar measurements evidently captured the MJO rainfall

evolution revealed in the much longer record (TRMM PR) satellite statistics.

The total rainfall was further divided into convective and stratiform types based on estimations from the *Revelle* radar and TRMM PR (Fig. 10). The 3-month *Revelle* radar estimates (Fig. 10a) show similar rainfall magnitudes as the long-term TRMM PR estimates (Fig. 10c) but display greater phase-to-phase variability compared to TRMM PR climatology. Both *Revelle* (Figs. 10a,b) and TRMM PR (Figs. 10c,d) precipitation estimates show that convective precipitation dominates the suppressed MJO phases (phases 5–7), but stratiform-type rainfall becomes substantial (40%–50%) in the MJO active phases (phases 2 and 3). XR14 related the growth of stratiform precipitation to moist mid- to upper-tropospheric conditions and strong deep tropospheric wind shear in active MJO phases. *Revelle* radar observations indicate that 80%–90% of the total precipitation in MJO suppressed phases (phases 5–7) falls as convective rain (Fig. 10b). This is reasonable, as the MJO suppressed phases were characterized by shallow and isolated convection as shown by XR14. In

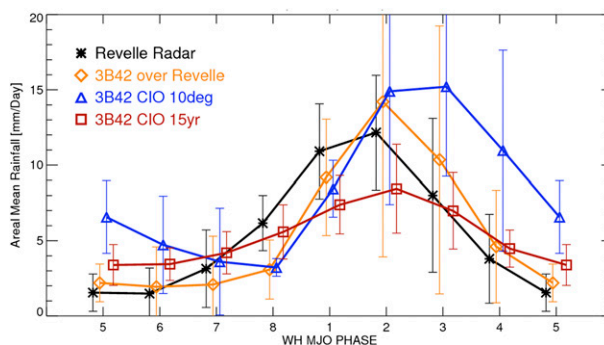


FIG. 9. Rainfall (areal mean) composites as a function of WH MJO phase from various rainfall estimation methods. Rainfall over the *Revelle* radar coverage area during October–December 2011 (when R/V *Revelle* was in station) is derived from the *Revelle* radar (black star) and TRMM 3B42 (orange diamond). TRMM 3B42 rainfall is also averaged over 5°S–5°N, 75°–85°E during October–December 2011 (blue triangle). Long-term (15 yr) TRMM PR (2A25) rainfall is averaged over 5°S–5°N, 75°–85°E during October–April from 1998 to 2012 (red square). Note that the 1–2–1 smoothing filter has been applied to these time series. Error bars pass the t test at 95% confidence interval based on daily means.

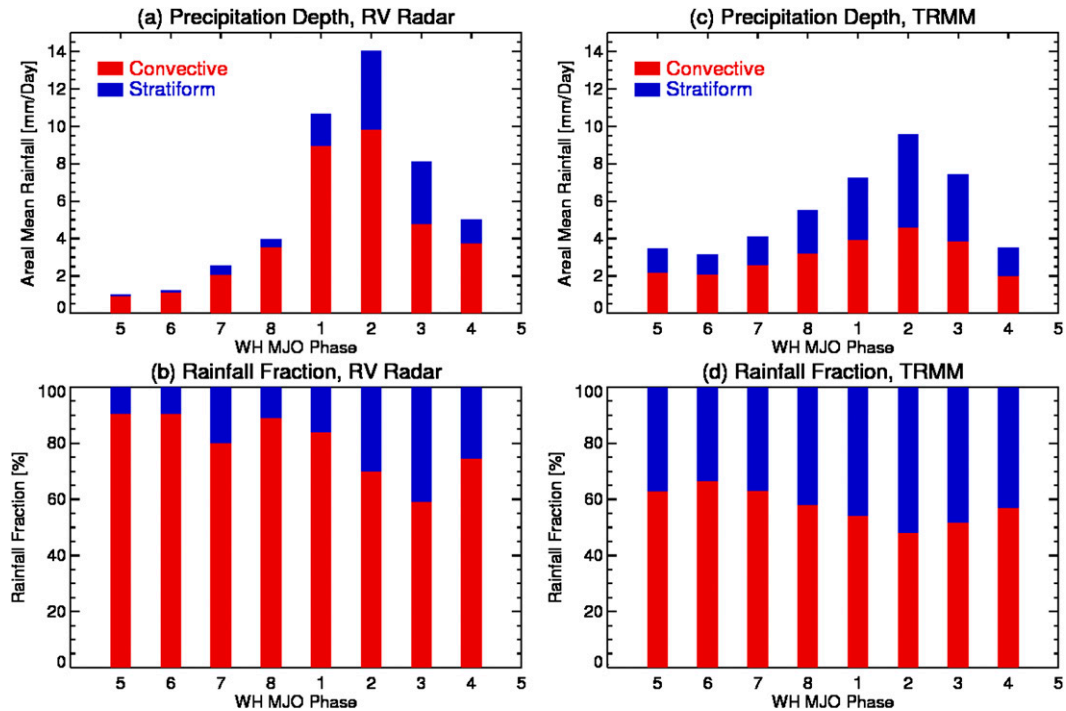


FIG. 10. Rainfall composites as a function of WH MJO phase contributed by convective and stratiform precipitation. (a),(b) *Revelle* radar statistics and (c),(d) TRMM PR statistics.

contrast, the TRMM PR climatology displays much lower convective rain fraction (50%–60%) in the suppressed phases (Fig. 10d).

Throughout the MJO life cycle, TRMM PR estimated lower convective rain fractions compared to *Revelle* radar. As has been mentioned previously, this is mainly due to the coarser resolution of the TRMM PR (4 km) relative to the *Revelle* radar (~2 km) such that the TRMM PR cannot adequately resolve various reflectivity gradients that are often characteristic of convection. Sensitivity tests show that the convective rain fractions are similar between *Revelle* radar and TRMM PR when the *Revelle* radar data are degraded to 4-km resolution. In addition, the TRMM PR may classify some of the isolated convection as stratiform precipitation owing to its lower sensitivity and reduced horizontal resolution compared to the *Revelle* radar. In fact, the identification of isolated convection poses a significant difficulty for partitioning algorithms (both for satellite and ground-based radars) because these echoes often have low reflectivities and weak horizontal gradients. While these isolated echoes are minor contributors to the total rainfall (~10%), it is important to properly classify them in order to understand the role of shallow isolated convection in MJO initiation. These types of echoes are present in 20%–30% of the radar observations from *Revelle* and are dominant during highly suppressed periods (XR14).

b. Rainfall distribution as a function of morphology and echo-top height

The total precipitation in each MJO phase was also broken down into fractional rainfall contributed from PFs in each of the four morphologies (Fig. 11). In general, suppressed MJO phases (e.g., phases 5–7) were characterized by sub-MCS rainfall, while active phases (e.g., phases 2 and 3) were dominated by the MCS rainfall. This is especially obvious in both the time series (Fig. 3) and composites (Figs. 11a,b) of *Revelle* radar measurements. *Revelle*-based composites also display more variability than the TRMM PR climatology. For example, *Revelle* radar measurements indicated that 60%–80% of the rainfall during suppressed phases (e.g., phases 5–7) came from sub-MCSs (Fig. 11b), while the TRMM PR analysis shows that only 30%–40% of rainfall fell from sub-MCSs (Fig. 11d). *Revelle*-based composites also show that the increase of MCS precipitation was quite sudden—for example, a rapid increase from phases 7 and 8 to phase 1 (Fig. 11a; also see the time series of the two MJO events in Fig. 3). Both the *Revelle* radar and TRMM PR indicated that MCSs contribute 75%–85% of the total precipitation during the MJO peak phase (e.g., phase 2; Figs. 11b and 11d). For active phases, TRMM PR climatology reveals that linear MCSs and nonlinear MCSs each contribute

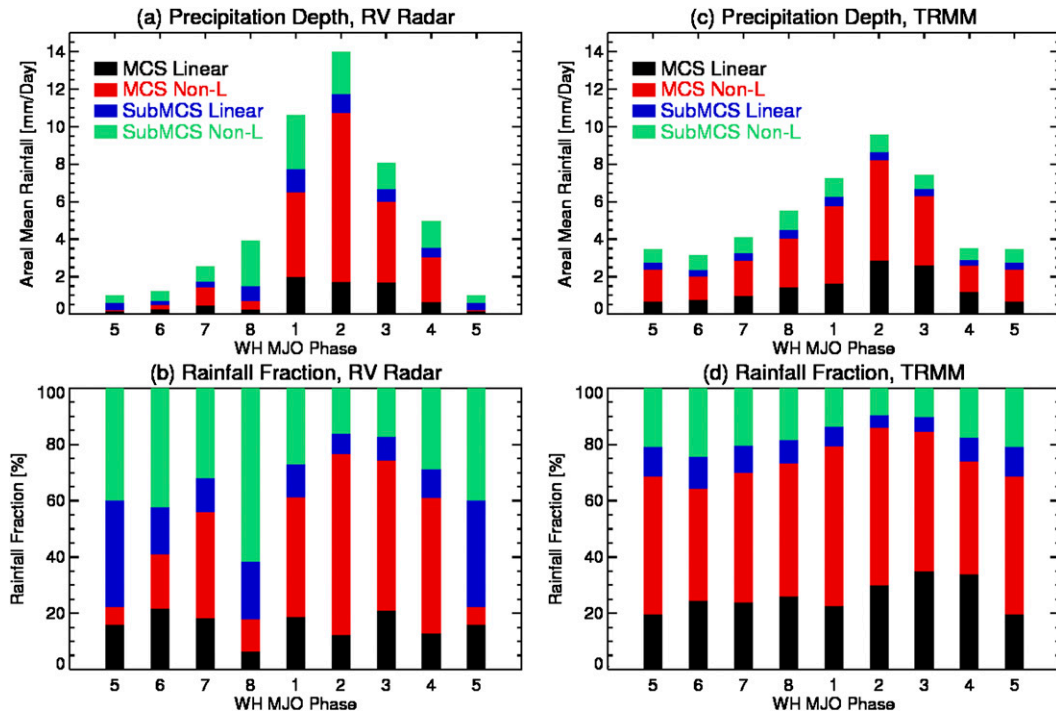


FIG. 11. Rainfall composites as a function of WH MJO phase contributed from PFs of different precipitation morphologies. (a),(b) *Revelle* radar measurements and (c),(d) TRMM PR statistics.

significantly to total rainfall ($\sim 40\%$; Fig. 11d). *Revelle* radar measurements indicate dominance of nonlinear MCS rainfall ($\sim 60\%$; Fig. 11b). The TRMM PR climatology also shows an increase of rainfall produced by linear MCSs from inactive to active phases (Figs. 11c,d), suggesting the frequent development of squall-line systems during active periods. As has been previously mentioned, the long swath (up to 1000 km in the study box) of the TRMM PR might enable PR to detect longer (or larger) squall-line systems compared to the *Revelle* radar (whose coverage was limited to 300 km in length).

Figure 12 indicates the rainfall amount and fractions in each MJO phase contributed from PFs with different echo-top heights [i.e., shallow (<5 km), middepth (5–8 km), and deep (>8 km)]. Basically, shallow PFs contribute a very small fraction of the total precipitation ($\sim 5\%$ from TRMM PR, $\sim 2\%$ from *Revelle*) throughout the MJO life cycle. Deep PFs produced the most rainfall (60%–80%) during all MJO phases, with 20%–40% of the rainfall contributed by PFs reaching heights at least to the midtroposphere. Both TRMM PR and *Revelle* statistics show that deep PFs contribute 15%–20% more rainfall in active periods than during MJO inactive periods (e.g., minimum at phases 5 and 6 and maximum at phase 2). This pattern of deep PF rainfall is exactly the same as that of MCS rainfall (Fig. 11). TRMM PR

(70%–85%; Fig. 12b) observed a higher fraction of rainfall originating from deep PFs compared to the *Revelle* radar (60%–75%; Fig. 12c), as well as MCS rainfall (Fig. 11). As was previously discussed, TRMM PR tended to retrieve more rainfall (in the climatological sense) than the *Revelle* radar (Fig. 8) for MCSs of similar convective intensities (Fig. 7). The reasons for these differences remain unclear.

6. Conclusions

This study used 3 months of shipborne radar observations during the 2011/12 DYNAMO field campaign along with a 15-yr climatology of TRMM PR measurements over the central Indian Ocean region to investigate convective morphologies, as well as convective intensity and rainfall contributions by each organizational category. This study first presented the convection–precipitation morphology characteristics of two major MJO events observed by the shipborne radar (*Revelle* radar) during DYNAMO. Time series of *Revelle* radar data indicated clear transitions of convective organization, intensity, and precipitation morphology from suppressed periods to active periods. The DYNAMO-based analysis was placed in the context of the substantially longer-term satellite (i.e., TRMM) climatology. This comparison indicates that the *Revelle* radar statistics are consistent with

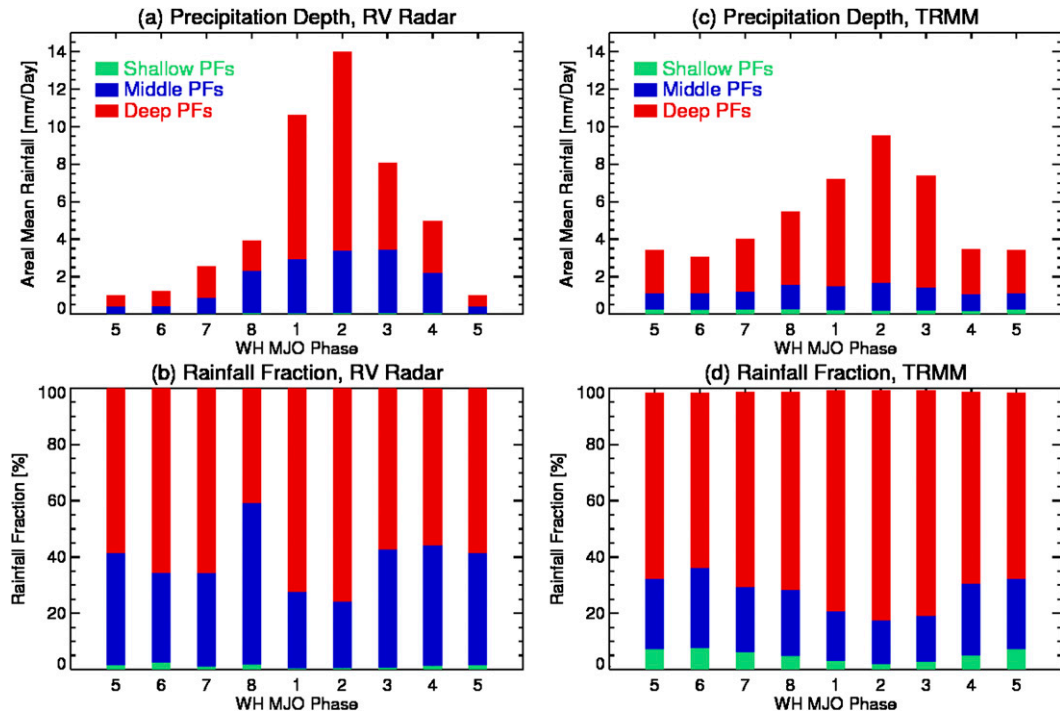


FIG. 12. As in Fig. 11, but for rainfall contributed from PFs of different 20-dBZ echo heights: shallow (<5 km), middle (between 5 and 8 km), and deep (>8 km).

those from the long-term TRMM PR record. Major findings in this study are as follows:

- 1) During the October and November 2011 MJO events observed by the *Revelle* radar, convective organization evolved from the sub-MCS organizational mode in suppressed periods to the MCS-dominated mode in active periods; this transition was consistent with those of the convective intensity and environmental conditions; MCSs were rare outside the MJO convective envelope.
- 2) The *Revelle* radar captured well the major climatological characteristics of MJO convection as indicated by comparison to the long-term TRMM PR statistics over the DYANMO array, including aspects of areal-mean rainfall (6–7 mm day⁻¹), distributions of convective intensities (20/30-dBZ echo-top heights), rainfall contributions from the four morphology categories, and variations of these parameters as a function of MJO phase.
- 3) Sub-MCSs (including both linear and nonlinear) were present 90% of the time (20% in linear and 70% in nonlinear mode) but only contributed roughly 30% of the total precipitation (10% in linear and 20% in nonlinear mode); nonlinear MCS events contribute much more volumetric rain (50%) compared to linear MCS events (20%), owing to their higher

- frequency of occurrence; however, these distributions also varied with MJO phase, with the highest sub-MCS rainfall fraction in suppressed phases (phases 5–7) and maximum MCS precipitation in active phases (phases 2 and 3).
- 4) Convective cells are deeper within MCSs (e.g., 20- and 30-dBZ echo-top heights are on average 2 km higher) compared to sub-MCSs; convective–stratiform rainfall fraction varies significantly with MJO phase, with the highest convective fraction (70%–80%) in suppressed phases and the largest stratiform fractions (40%–50%) in active phases; similarly, active phases are also characterized by maximum fraction of rainfall generated by deep convective cells.
- 5) There are differences between the statistics derived from *Revelle* radar and TRMM PR, such as convective–stratiform rainfall fraction (e.g., *Revelle* radar indicated a mean stratiform fraction of 30% compared to 45% for TRMM PR); TRMM PR composites indicate linear MCS rainfall increases after MJO onset and produces similar rainfall contributions to nonlinear MCSs; however, the *Revelle* radar statistics showed the clear dominance of nonlinear MCS rainfall (more than twice that of linear MCSs).
- 6) The TRMM PR estimated lower convective rain fractions compared to the *Revelle* radar. We suggest this is mainly due to the coarser resolution of the

TRMM PR (4 km) relative to the *Revelle* radar (~2 km) such that the TRMM PR cannot adequately resolve various reflectivity gradients that are often characteristic of convection. When the *Revelle* radar data were degraded to 4-km resolution, convective fractions between the two platforms were very similar.

Acknowledgments. This research was supported by the National Science Foundation DYNAMO Project Grant AGS-1063928. We thank Edward Zipser and Chuntao Liu for providing the TRMM precipitation feature data. We also thank the entire crew of the R/V *Revelle* for their excellent support and *Revelle* Chief Scientist James Moum for his dedication and leadership. We are also grateful to Robert Houze, Courtney Schumacher, Masaki Katsumata and their research groups for data analysis and radar science discussions. We thank Ramesh Kakar, John Gerlach Walter Petersen, and the late Arthur Hou (all NASA) for making the NASA TOGA radar available for DYNAMO. Chidong Zhang was the lead principle investigator for DYNAMO and we are grateful for his excellent leadership of the project.

REFERENCES

- Alexander, G. D., and G. S. Young, 1992: The relationship between EMEX mesoscale precipitation feature properties and their environmental characteristics. *Mon. Wea. Rev.*, **120**, 554–564, doi:10.1175/1520-0493(1992)120<0554:TRBEMP>2.0.CO;2.
- Awaka, J., T. Iguchi, and K. Okamoto, 2009: TRMM PR standard algorithm 2A23 and its performance on bright band detection. *J. Meteor. Soc. Japan*, **87A**, 31–52, doi:10.2151/jmsj.87A.31.
- Barnes, G. M., and K. Seickman, 1984: The environment of fast- and slow-moving tropical mesoscale convective cloud lines. *Mon. Wea. Rev.*, **112**, 1782–1794, doi:10.1175/1520-0493(1984)112<1782:TEOFAS>2.0.CO;2.
- Bechtold, P., M. Köhler, T. Jung, F. Doblas-Reyes, M. Leutbecher, M. J. Rodwell, F. Vitart, and G. Balsamo, 2008: Advances in simulating atmospheric variability with the ECMWF model: From synoptic to decadal time-scales. *Quart. J. Roy. Meteor. Soc.*, **134**, 1337–1351, doi:10.1002/qj.289.
- Bladé, I., and D. L. Hartmann, 1993: Tropical intraseasonal oscillations in a simple nonlinear model. *J. Atmos. Sci.*, **50**, 2922–2939, doi:10.1175/1520-0469(1993)050<2922:TIOIAS>2.0.CO;2.
- Cheng, C.-P., and R. A. Houze Jr., 1979: The distribution of convective and mesoscale precipitation in GATE radar echo patterns. *Mon. Wea. Rev.*, **107**, 1370–1381, doi:10.1175/1520-0493(1979)107<1370:TDOCAM>2.0.CO;2.
- Cifelli, R., S. W. Nesbitt, S. A. Rutledge, W. A. Petersen, and S. Yuter, 2007: Radar characteristics of precipitation features in the EPIC and TEPPS regions of the east Pacific. *Mon. Wea. Rev.*, **135**, 1576–1595, doi:10.1175/MWR3340.1.
- Feng, Z., S. A. McFarlane, C. Schumacher, S. Ellis, J. Comstock, and N. Bharadwaj, 2014: Constructing a merged cloud-precipitation radar dataset for tropical convective clouds during the DYNAMO/AMIE Experiment at Addu Atoll. *J. Atmos. Tech.*, **31**, 1021–1042, doi:10.1175/JTECH-D-13-00132.1.
- Gamache, J. F., and R. A. Houze, 1983: Water budget of a mesoscale convective system in the tropics. *J. Atmos. Sci.*, **40**, 1835–1850, doi:10.1175/1520-0469(1983)040<1835:WBOAMC>2.0.CO;2.
- Gottschalck, J., P. E. Roundy, C. J. Schreck III, A. Vintzileos, and C. Zhang, 2013: Large-scale atmospheric and oceanic conditions during the 2011–12 DYNAMO field campaign. *Mon. Wea. Rev.*, **141**, 4173–4196, doi:10.1175/MWR-D-13-00022.1.
- Guy, N., and D. P. Jorgensen, 2014: Kinematic and precipitation characteristics of convective systems observed by airborne doppler radar during the life cycle of a Madden–Julian oscillation in the Indian Ocean. *Mon. Wea. Rev.*, **142**, 1385–1402, doi:10.1175/MWR-D-13-00252.1.
- Hendon, H. H., and B. Liebmann, 1990: The intraseasonal (30–50 day) oscillation of the Australian summer monsoon. *J. Atmos. Sci.*, **47**, 2909–2923, doi:10.1175/1520-0469(1990)047<2909:TIDOOT>2.0.CO;2.
- Houze, R. A., Jr., 1977: Structure and dynamics of a tropical squall-line system. *Mon. Wea. Rev.*, **105**, 1540–1567, doi:10.1175/1520-0493(1977)105<1540:SADOAT>2.0.CO;2.
- , 1989: Observed structure of mesoscale convective systems and implications for large-scale heating. *Quart. J. Roy. Meteor. Soc.*, **115**, 425–461, doi:10.1002/qj.49711548702.
- , and E. N. Rappaport, 1984: Air motions and precipitation structure of an early summer squall line over the eastern tropical Atlantic. *J. Atmos. Sci.*, **41**, 553–574, doi:10.1175/1520-0469(1984)041<0553:AMAPSO>2.0.CO;2.
- Hu, Q., and D. A. Randall, 1994: Low-frequency oscillations in radiative-convective systems. *J. Atmos. Sci.*, **51**, 1089–1099, doi:10.1175/1520-0469(1994)051<1089:LFOIRC>2.0.CO;2.
- Huffman, G. J., and Coauthors, 2007: The TRMM Multisatellite Precipitation Analysis (TMPA): Quasi-global, multiyear, combined-sensor precipitation estimates at fine scales. *J. Hydrometeorol.*, **8**, 38–55, doi:10.1175/JHM560.1.
- Hung, M.-P., J.-L. Lin, W. Wang, D. Kim, T. Shinoda, and S. J. Weaver, 2013: MJO and convectively coupled equatorial waves simulated by CMIP5 climate models. *J. Climate*, **26**, 6185–6214, doi:10.1175/JCLI-D-12-00541.1.
- Iguchi, T., T. Kozu, J. Kwiatkowski, R. Meneghini, J. Awaka, and K. Okamoto, 2009: Uncertainties in the rain profiling algorithm for the TRMM precipitation radar. *J. Meteor. Soc. Japan*, **87A**, 1–30, doi:10.2151/jmsj.87A.1.
- Johnson, R. H., 1984: Partitioning tropical heat and moisture budgets into cumulus and mesoscale components: Implications for cumulus parameterization. *Mon. Wea. Rev.*, **112**, 1590–1601, doi:10.1175/1520-0493(1984)112<1590:PTHAMB>2.0.CO;2.
- , and P. E. Ciesielski, 2013: Structure and properties of Madden–Julian oscillations deduced from DYNAMO sounding arrays. *J. Atmos. Sci.*, **70**, 3157–3179, doi:10.1175/JAS-D-13-065.1.
- , S. L. Aves, P. E. Ciesielski, and T. D. Keenan, 2005: Organization of oceanic convection during the onset of the 1998 East Asian summer monsoon. *Mon. Wea. Rev.*, **133**, 131–148, doi:10.1175/MWR-2843.1.
- Keenan, T. D., and R. E. Carbone, 1992: A preliminary morphology of precipitation systems in tropical northern Australia. *Quart. J. Roy. Meteor. Soc.*, **118**, 283–326, doi:10.1002/qj.49711850406.
- , and S. A. Rutledge, 1993: Mesoscale characteristics of monsoonal convection and associated stratiform precipitation. *Mon. Wea. Rev.*, **121**, 352–374, doi:10.1175/1520-0493(1993)121<0352:MCOMCA>2.0.CO;2.
- Kemball-Cook, S. R., and B. C. Weare, 2001: The onset of convection in the Madden–Julian oscillation. *J. Climate*, **14**, 780–793, doi:10.1175/1520-0442(2001)014<0780:TOOCIT>2.0.CO;2.

- Kim, D., and Coauthors, 2009: Application of MJO simulation diagnostics to climate models. *J. Climate*, **22**, 6413–6436, doi:10.1175/2009JCLI3063.1.
- Kummerow, C., W. Barnes, T. Kozu, J. Shiue, and J. Simpson, 1998: The Tropical Rainfall Measuring Mission (TRMM) sensor package. *J. Atmos. Oceanic Technol.*, **15**, 809–817, doi:10.1175/1520-0426(1998)015<0809:TTRMMT>2.0.CO;2.
- Lau, W. K.-M., 2012: El Niño Southern Oscillation connection. *Intraseasonal Variability of the Atmosphere–Ocean Climate System*, 2nd ed., W. K.-M. Lau and D. E. Waliser, Eds., Springer, 297–334.
- , and P. H. Chan, 1986: Aspects of the 40–50 day oscillation during the northern summer as inferred from outgoing long-wave radiation. *Mon. Wea. Rev.*, **114**, 1354–1367, doi:10.1175/1520-0493(1986)114<1354:AOTDOD>2.0.CO;2.
- , and D. E. Waliser, 2005: *Intraseasonal Variability in the Atmosphere–Ocean Climate System*. Praxis, 436 pp.
- , and H.-T. Wu, 2010: Characteristics of precipitation, cloud, and latent heating associated with the Madden–Julian oscillation. *J. Climate*, **23**, 504–518, doi:10.1175/2009JCLI2920.1.
- Lawrence, D. M., and P. J. Webster, 2002: The boreal summer intraseasonal oscillation: Relationship between northward and eastward movement of convection. *J. Atmos. Sci.*, **59**, 1593–1606, doi:10.1175/1520-0469(2002)059<1593:TBSIOR>2.0.CO;2.
- Leary, C. A., 1984: Precipitation structure of the cloud clusters in a tropical easterly wave. *Mon. Wea. Rev.*, **112**, 313–325, doi:10.1175/1520-0493(1984)112<0313:PSOTCC>2.0.CO;2.
- LeMone, M. A., 1983: Momentum transport by a line of cumulonimbus. *J. Atmos. Sci.*, **40**, 1815–1834, doi:10.1175/1520-0469(1983)040<1815:MTBALO>2.0.CO;2.
- , G. M. Barnes, and E. J. Zipser, 1984: Momentum flux by lines of cumulonimbus over the tropical ocean. *J. Atmos. Sci.*, **41**, 1914–1932, doi:10.1175/1520-0469(1984)041<1914:MFBLOC>2.0.CO;2.
- , E. J. Zipser, and S. B. Trier, 1998: The role of environmental shear and thermodynamic conditions in determining the structure and evolution of mesoscale convective systems during TOGA COARE. *J. Atmos. Sci.*, **55**, 3493–3518, doi:10.1175/1520-0469(1998)055<3493:TROESA>2.0.CO;2.
- L’Heureux, M. L., and R. W. Higgins, 2008: Boreal winter links between the Madden–Julian oscillation and the Arctic Oscillation. *J. Climate*, **21**, 3040–3050, doi:10.1175/2007JCLI1955.1.
- Liebmann, B., H. Hendon, and J. Glick, 1994: The relationship between tropical cyclones of the western Pacific and Indian oceans and the Madden–Julian Oscillation. *J. Meteor. Soc. Japan*, **72**, 401–411.
- Lin, H., G. Brunet, and J. Derome, 2009: An observed connection between the North Atlantic Oscillation and the Madden–Julian oscillation. *J. Climate*, **22**, 364–380, doi:10.1175/2008JCLI2515.1.
- Lin, J., B. Mapes, M. Zhang, and M. Newman, 2004: Stratiform precipitation, vertical heating profiles, and the Madden–Julian oscillation. *J. Atmos. Sci.*, **61**, 296–309, doi:10.1175/1520-0469(2004)061<0296:SPVHPA>2.0.CO;2.
- , and Coauthors, 2006: Tropical intraseasonal variability in 14 IPCC AR4 climate models. Part I: Convective signals. *J. Climate*, **19**, 2665–2690, doi:10.1175/JCLI3735.1.
- Liu, C., and E. Zipser, 2013: Regional variation of morphology of organized convection in the tropics and subtropics. *J. Geophys. Res. Atmos.*, **118**, 453–466, doi:10.1029/2012JD018409.
- , —, D. J. Cecil, S. W. Nesbitt, and S. Sherwood, 2008: A cloud and precipitation feature database from nine years of TRMM observations. *J. Appl. Meteor.*, **47**, 2712–2728, doi:10.1175/2008JAMC1890.1.
- Madden, R. A., and P. R. Julian, 1971: Detection of a 40–50 day oscillation in the zonal wind in the tropical Pacific. *J. Atmos. Sci.*, **28**, 702–708, doi:10.1175/1520-0469(1971)028<0702:DOADOI>2.0.CO;2.
- , and —, 1972: Description of global-scale circulation cells in the tropics with a 40–50 day period. *J. Atmos. Sci.*, **29**, 1109–1123, doi:10.1175/1520-0469(1972)029<1109:DOGSCC>2.0.CO;2.
- Maloney, E. D., and D. L. Hartmann, 2000: Modulation of eastern North Pacific hurricanes by the Madden–Julian oscillation. *J. Climate*, **13**, 1451–1460, doi:10.1175/1520-0442(2000)013<1451:MOENPH>2.0.CO;2.
- Medioni, G., M.-S. Lee, and C. K. Tang, 2000: *A Computational Framework for Segmentation and Grouping*. Elsevier, 260 pp.
- Moncrieff, M. W., and J. S. A. Green, 1972: The propagation and transfer properties of steady convective overturning in shear. *Quart. J. Roy. Meteor. Soc.*, **98**, 336–352, doi:10.1002/qj.49709841607.
- Morita, J., Y. N. Takayabu, S. Shige, and Y. Kodama, 2006: Analysis of rainfall characteristics of the Madden–Julian oscillation using TRMM satellite data. *Dyn. Atmos. Oceans*, **42**, 107–126, doi:10.1016/j.dynatmoce.2006.02.002.
- Moum, J. N., and Coauthors, 2014: Air–sea interactions from the westerly wind burst events during the November 2011 MJO in the Indian Ocean. *Bull. Amer. Meteor. Soc.*, **95**, 1185–1199, doi:10.1175/BAMS-D-12-00225.1.
- Nesbitt, S. W., E. J. Zipser, and D. J. Cecil, 2000: A census of precipitation features in the tropics using TRMM: Radar, ice scattering, and lightning observations. *J. Climate*, **13**, 4087–4106, doi:10.1175/1520-0442(2000)013<4087:ACOPFI>2.0.CO;2.
- , R. Cifelli, and S. A. Rutledge, 2006: Storm morphology and rainfall characteristics of TRMM precipitation features. *Mon. Wea. Rev.*, **134**, 2702–2721, doi:10.1175/MWR3200.1.
- Oye, D., and M. Case, 1995: REORDER: A program for gridding radar data: Installation and use manual for the UNIX version. NCAR/ATD, 30 pp. [Available online at <https://www.eol.ucar.edu/system/files/unixreorder.pdf>.]
- Petersen, W. A., S. A. Rutledge, and R. E. Orville, 1996: Cloud-to-ground lightning observations from TOGA COARE: Selected results and lightning location algorithms. *Mon. Wea. Rev.*, **124**, 602–620, doi:10.1175/1520-0493(1996)124<0602:CTGLOF>2.0.CO;2.
- Powell, S., and R. A. Houze Jr., 2014: The cloud population and onset of the Madden–Julian Oscillation over the Indian Ocean during DYNAMO-AMIE. *J. Geophys. Res.*, **118**, 11 979–11 995, doi:10.1002/2013JD020421.
- Rickenbach, T. M., and S. A. Rutledge, 1998: Convection in TOGA COARE: Horizontal scale, morphology, and rainfall production. *J. Atmos. Sci.*, **55**, 2715–2729, doi:10.1175/1520-0469(1998)055<2715:CITCHS>2.0.CO;2.
- Riley, E. M., B. E. Mapes, and S. N. Tulich, 2011: Clouds associated with the Madden–Julian oscillation: A new perspective from *CloudSat*. *J. Atmos. Sci.*, **68**, 3032–3051, doi:10.1175/JAS-D-11-030.1.
- Rowe, A. K., and R. A. Houze Jr., 2014: Microphysical characteristics of MJO convection over the Indian Ocean during DYNAMO. *J. Geophys. Res. Atmos.*, **119**, 2543–2554, doi:10.1002/2013JD020799.
- Saxen, T. R., and S. A. Rutledge, 1998: Surface fluxes and boundary layer recovery in TOGA COARE: Sensitivity to convective organization. *J. Atmos. Sci.*, **55**, 2763–2781, doi:10.1175/1520-0469(1998)055<2763:SFABLR>2.0.CO;2.
- Short, D. A., P. A. Kucera, B. S. Ferrier, J. C. Gerlach, S. A. Rutledge, and O. W. Thiele, 1997: Shipboard radar rainfall

- patterns within the TOGA COARE IFA. *Bull. Amer. Meteor. Soc.*, **78**, 2817–2836, doi:10.1175/1520-0477(1997)078<2817:SRRPWT>2.0.CO;2.
- Steiner, M., R. A. Houze Jr., and S. E. Yuter, 1995: Climatological characterization of three-dimensional storm structure from operational radar and rain gauge data. *J. Appl. Meteor.*, **34**, 1978–2007, doi:10.1175/1520-0450(1995)034<1978:CCOTDS>2.0.CO;2.
- Szoke, E. J., and E. J. Zipser, 1986: A radar study of convective cells in mesoscale systems in GATE. Part II: life cycles of convective cells. *J. Atmos. Sci.*, **43**, 199–218, doi:10.1175/1520-0469(1986)043<0199:ARSOCC>2.0.CO;2.
- Tao, W. K., J. Simpson, C.-H. Sui, B. Ferrier, S. Lang, J. Scala, M.-D. Chou, and K. Pickering, 1993: Heating, moisture, and water budgets of tropical and midlatitude squall lines: Comparisons and sensitivity to longwave radiation. *J. Atmos. Sci.*, **50**, 673–690, doi:10.1175/1520-0469(1993)050<0673:HMAWBO>2.0.CO;2.
- Thompson, D. B., and P. E. Roundy, 2013: The relationship between the Madden–Julian oscillation and U.S. violent tornado outbreaks in the spring. *Mon. Wea. Rev.*, **141**, 2087–2095, doi:10.1175/MWR-D-12-00173.1.
- Tromeur, E., and W. B. Rossow, 2010: Interaction of tropical deep convection with the large-scale circulation in the MJO. *J. Climate*, **23**, 1837–1853, doi:10.1175/2009JCLI3240.1.
- Tung, W.-W., and M. Yanai, 2002: Convective momentum transport observed during the TOGA COARE IOP. Part I: General features. *J. Atmos. Sci.*, **59**, 1857–1871, doi:10.1175/1520-0469(2002)059<1857:CMTODT>2.0.CO;2.
- Vitart, F., and F. Molteni, 2010: Simulation of the Madden–Julian oscillation and its teleconnections in the ECMWF forecast system. *Quart. J. Roy. Meteor. Soc.*, **136**, 842–855, doi:10.1002/qj.623.
- Wheeler, M., and H. H. Hendon, 2004: An all-season real-time multivariate MJO index: Development of an index for monitoring and prediction. *Mon. Wea. Rev.*, **132**, 1917–1932, doi:10.1175/1520-0493(2004)132<1917:AARMMI>2.0.CO;2.
- Wu, X., and M. Yanai, 1994: Effects of vertical wind shear on the cumulus transport of momentum: Observations and parameterization. *J. Atmos. Sci.*, **51**, 1640–1660, doi:10.1175/1520-0469(1994)051<1640:EOVWSO>2.0.CO;2.
- Xu, W., and E. J. Zipser, 2012: Regime variations among continental, monsoon, and oceanic deep convection over the tropics. *Geophys. Res. Lett.*, **39**, L07802, doi:10.1029/2012GL051242.
- , and S. A. Rutledge, 2014: Convective characteristics of the Madden–Julian oscillation over the central Indian Ocean observed by shipborne radar during DYNAMO. *J. Atmos. Sci.*, **71**, 2859–2877, doi:10.1175/JAS-D-13-0372.1.
- Yoneyama, K., C. Zhang, and C. N. Long, 2013: Tracking pulses of the Madden–Julian oscillation. *Bull. Amer. Meteor. Soc.*, **94**, 1871–1891, doi:10.1175/BAMS-D-12-00157.1.
- Zhang, C., 2005: Madden-Julian Oscillation. *Rev. Geophys.*, **43**, RG2003, doi:10.1029/2004RG000158.
- , 2013: Madden–Julian oscillation: Bridging weather and climate. *Bull. Amer. Meteor. Soc.*, **94**, 1849–1870, doi:10.1175/BAMS-D-12-00026.1.
- Zipser, E. J., 1977: Mesoscale and convective-scale downdraughts as distinct components of squall-line circulation. *Mon. Wea. Rev.*, **105**, 1568–1589, doi:10.1175/1520-0493(1977)105<1568:MACDAD>2.0.CO;2.
- , 1994: Deep cumulonimbus cloud systems in the tropics with and without lightning. *Mon. Wea. Rev.*, **122**, 1837–1851, doi:10.1175/1520-0493(1994)122<1837:DCCSIT>2.0.CO;2.
- , R. J. Meitin, and M. A. LeMone, 1981: Mesoscale motion fields associated with a slowly moving GATE convective band. *J. Atmos. Sci.*, **38**, 1725–1750, doi:10.1175/1520-0469(1981)038<1725:MMFAWA>2.0.CO;2.
- Zuluaga, M. D., and R. A. Houze Jr., 2013: Evolution of the population of precipitating convective systems over the equatorial Indian Ocean in active phases of the Madden–Julian oscillation. *J. Atmos. Sci.*, **70**, 2713–2725, doi:10.1175/JAS-D-12-0311.1.